CHEMISTRY OF MATERIALS

pubs.acs.org/cm

Article

Metal–Organic Polyhedra and Metal–Organic Frameworks: Understanding How Discrete Versus Extended Structure Impacts Surface Areas and Pore Size Distributions

Heshali K. Welgama, Anish Avasthi, and Timothy R. Cook*

Cite This: *Chem. Mater.* 2024, 36, 4185–4195

Read Online

ACCESS | Metrics & More | Article Recommendations | Supporting Information

ABSTRACT: Certain discrete metal–organic polyhedra (MOPs) contain pores that also appear in extended metal–organic frameworks (MOFs) and MOP-based supramolecular frameworks. Here, we have selected a library of three MOPs (ZrMOP, CuMOP, and PdMOP) and their corresponding MOFs with analogous pores (UiO-66, HKUST-1, and the Co Sponge) to understand how parameters related to their sorption behavior differ. Specifically, we report the BET areas and pore size distributions for all six species. The BET areas for the MOPs follow the same trend as those for their MOF counterparts, with the highest shown by the ZrMOP (379 m^2/g) and UiO-66 (1110 m^2/g) pair. A discussion of the Zr-based materials includes comparisons to a known ZrMOP-based supramolecular framework that maintains extrinsic porosity via noncovalent interactions. The lowest areas were measured for the PdMOP (33 m^2/g) and Co Sponge (80 m^2/g) pair, a ramification of a phase transition that occurs during activation. Additionally, pore size distribution measurements suggest that the lower BET areas likely result from inaccessible internal cavities. Although the ZrMOP has the highest area per pore, its BET area is not as high as that of UiO-66 because the pores in an MOF share building blocks, greatly reducing the mass required to support a given number of pores, and the pores pack more tightly in space. MOFs are also more resilient to structural collapse upon activation, though we highlight some interesting examples for a loss of crystallinity that can increase the BET area of certain MOPs. Supramolecular chemistry can further enhance the properties of MOPs, where careful ligand or cage design can promote noncovalent interactions to enforce additional extrinsic porosity. Although MOFs remain top candidates for bulk storage and uptake due to their gravimetric and volumetric areas, for applications in thin films and membranes for separations chemistry, highly dispersed pores are desirable and the higher area per pore of MOPs is advantageous.

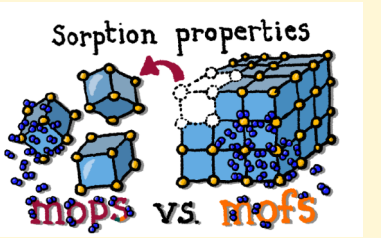

INTRODUCTION

Coordination-driven self-assembly between precursors containing Lewis-acidic groups (acceptors) and Lewis-basic groups (donors) can give rise to discrete structures or extended frameworks.[1,2] The structural outcome of these self-assembly reactions is governed by factors that include the number of binding sites on the metal center (or metal cluster), their orientation, the number of Lewis-basic sites on the ligand, and the directionalities of the coordination vectors.[1] Metal–organic polyhedra (MOPs) are discrete structures that often have capping ligands to enforce convergent geometries. In contrast, metal–organic frameworks (MOFs) contain nodes and bridging ligands that bind to give divergent geometries that extend in either two or three dimensions.

Both MOPs and MOFs are attractive primarily due to their porous nature,[3,4] which motivates their functional applications, for example, as materials for capacitive deionization.[5−7] In certain cases, the same pore may appear in both an MOP and an MOF, with the MOP representing a single, discrete cavity that is repeated into an extended network within the corresponding MOF. In addition to their related but unique structures, there are a few other differences between these two materials. With MOPs, it is possible to have a molecular-level stoichiometric control over the synthesis and postsynthetic modifications to precisely tune structural and functional properties.[8,9] Since they are molecules, MOPs may also be soluble in a range of different solvents,[10−12] which improves their solution processability, a property that can be very useful when incorporating MOPs as filler materials into membranes and thin films.[13−15] MOPs may also be characterized using solution-phase techniques such as nuclear magnetic resonance (NMR),[16] mass spectrometry,[8] UV–vis spectroscopy,[12] and dynamic light scattering[17] (DLS). In contrast, MOFs are typically characterized by techniques such as PXRD, TGA, and microscopy, to name a few.

Although both MOFs and MOPs were first introduced around the same time and the two fields are heavily linked, their development has largely been orthogonal. Some groups that have made significant contributions to MOF chemistry

Received: November 28, 2023
Revised: March 26, 2024
Accepted: March 27, 2024
Published: April 16, 2024

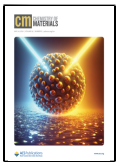

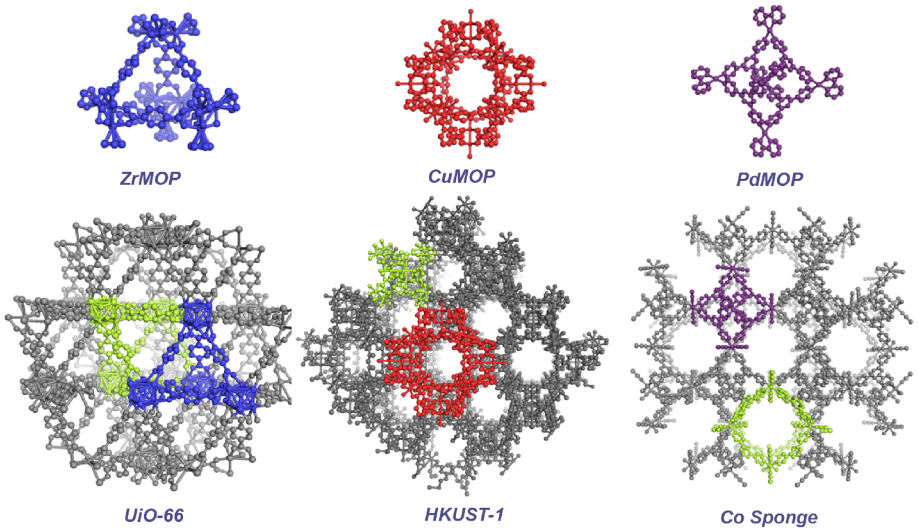

Figure 1. Crystallographic structures of ZrMOP-1 (CCDC 950330),[25] UiO-66 (CCDC 733458),[26] CuMOP-1 (CCDC 1212282),[27] HKUST-1 (CCDC 112954),[28] PdMOP-1 (CCDC 1208789),[29] and Co Sponge (CCDC 766604.[30] The fragments of the MOFs that match the MOPs are color matched. All MOFs also contain additional pores or channels that do not match the respective MOPs, shown in green. HKUST-1 and Co Sponge structures have a third pore that is different from their analogous MOPs, in addition to the representative ones shown in green.

have translated their expertise to discrete systems, such as Yaghi,[18] Zhou,[9] and Bloch[19] and their characterizations and functional applications overlap with how these groups study related frameworks. Other MOP research was developed in laboratories with significant organic synthetic and/or supramolecular expertise, for example, Stang,[20] Nitschke,[21] Fujita,[22] Raymond,[23] and Mukherjee[24] where characterization and reactivity chemistry is clearly inspired by small molecule methods. Although studies of MOFs have greatly outpaced their discrete analogues, a growing interest in MOPs is evidenced by an increasing number of novel cages,[31,32] and strategies to improve their stability[33−35] as well as their applicability in gas storage,[36,37] catalysis,[38,39] separations,[40−42] and biological[43,44] applications.

For applications that require porosity, MOFs have dominated contemporary research due to their high gravimetric surface areas,[45] with experimentally measured values over 7000 m^2/g being reported.[46,47] The surface areas of certain MOPs can approach that of some MOFs,[19,48,49] though in general, the values measured for discrete cages are smaller. In general, the extrinsic porosity of simple MOPs is often very low for two reasons. First, solid-state packing is most efficient when interparticle voids are minimized through close contacts and second, extended structure is often lost upon activation/desolvation.[50] Both deleterious effects can be addressed by the design of MOPs that can act as building blocks for larger supramolecular frameworks, where extrinsic porosity is introduced between the cage subunits. For example, by installing hydrogen-bonding carboxylate groups to zeolite-like cubic cages, hydrogen gas uptake was significantly enhanced.[51] Hydrogen bonding can be further augmented by hydrophobic interactions, as illustrated by Ni and Co MOPs whose extrinsic porosity contributed to cavity-confined catalysis for [3 + 2] coupling reactions.[49] In some cases, counterions are directly incorporated into the supramolecular network, helping to maintain extrinsic porosity.[52,53] The clever design of a family of CuMOPs with tripodal carboxylate ligands resulted in extended supramolecular frameworks enforced by van der Waals where extrinsic porosity was primarily responsible for gas sorption.[50]

Even for systems that lack extrinsic porosity, the differences in surface areas are somewhat intuitive as each pore in an MOP represents an entire molecule, whereas in an MOF, the pores can share building blocks, reducing the overall mass for a given number of pores. In addition, in MOFs and MOP-based supramolecular frameworks, there is often more than one type of pore. For example, UiO-66 contains tetrahedral pores that can be replicated in a discrete MOP, but the packing in the MOF also creates octahedral pores. In the solid-state packing of amine-functionalized ZrMOPs, an extended supramolecular framework introduces similar pores to UiO-66.[53] In HKUST-1, there are two larger cuboctahedral pore types and a smaller pore type with a truncated tetrahedral geometry.[54] In the Co Sponge, there are three total pores.[55] We became interested in a deeper understanding of these effects. To quantify how sorption properties vary between discrete and extended structures, we identified a library of three MOPs along with three MOFs selected as pairs with similar or identical pores. Here, we have investigated ZrMOP ($M_{12}L_6$) reported by Yuan et al.[25] compared to UiO-66,[26] CuMOP ($M_{24}L_{24}$) reported by Yaghi et al.[27] compared to HKUST-1,[28] and PdMOP (M_6L_4)[29] reported by Fujita et al. compared to their Co Sponge (Figure 1).[30] The Co Sponge is known to undergo a phase transition at the surface of single crystals when solvent molecules are removed to form a semiamorphous material.[55] We included this material in our study, as this transformation was reported to be confined to the surface without impacting the bulk structure. Nitrogen sorption isotherms were collected, and the Brunauer−Emmett−Teller (BET) theory was used to calculate BET areas and pore size distributions to frame a discussion of why these materials differ so significantly, despite structurally similar building blocks and analogous pores.

EXPERIMENTAL SECTION

Materials. Zirconocene dichloride 99% (Strem Chemicals), zirconium(IV) chloride >99.5% (Alfa Aeser), copper(II) acetate monohydrate 98−102% (Beantown Chemicals), copper(II) nitrate

https://doi.org/10.1021/acs.chemmater.3c03020
Chem. Mater. 2024, 36, 4185−4195

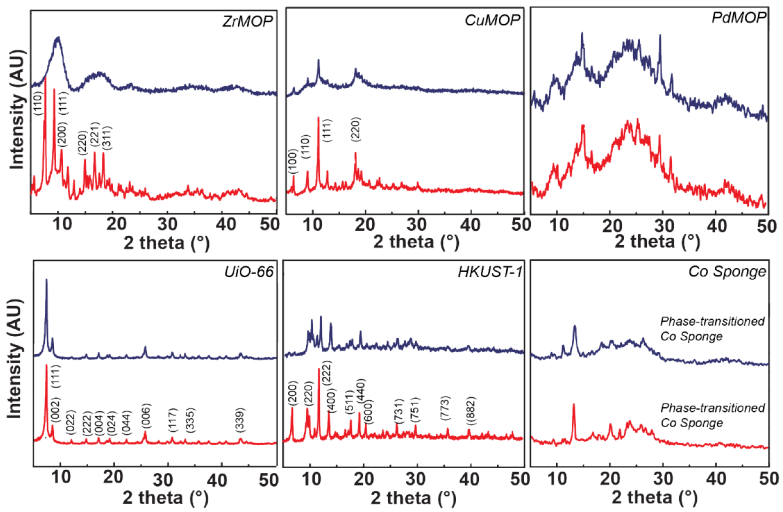

Figure 2. PXRD patterns of MOP and MOF samples, as-synthesized (red) and after N_2 sorption experiments (blue).

2.5 hydrate 98−102% (J.T. Baker), palladium(II) chloride 99% (Strem Chemicals), cobalt thiocyanate >98% (Alfa Aeser), 1,4-benzenedicarboxylic acid (terephthalic acid) > 99% (TCI Chemicals), 1,3-benzenedicarboxylic acid (isophthalic acid) 99% (Alfa Aeser), 1,3,5-benzenedicarboxylic acid (trimesic acid) > 99% (Alfa Aeser), 2,2′-bipyridine 99.6% (Chem Impex Int'l), silver nitrate >99.7% (Fisher Scientific), 2,4,6-tris(4-pyridyl)-1,3,5-triazine (TPT) > 97% (TCI Chemicals). All starting materials, reagents, and solvents were used as received without further purification.

Characterization. X-ray diffraction (PXRD) patterns were collected from a Rigaku Ultima IV X-ray diffractometer equipped with a Cu source and operated at 1.76 kW of power (40 kV, 44 mA). Diffraction patterns were measured over a 2θ range of 5−50° at a scan rate of 2° min^{-1}. ^1H NMR spectra were acquired by using a Bruker AVANCE NEO 500 spectrometer. Chemical shifts are reported in parts per million (ppm) referenced to residual solvent peaks. Thermogravimetric analysis (TGA) experiments were carried out using a PerkinElmer TGA 8000 instrument and platinum pans (Instrument Specialists Incorporation), by heating the samples from 30 to 700 °C at a rate of 5 °C/min under N_2 flow. Fourier transform infrared (FTIR) spectra were acquired from a PerkinElmer 1760 FTIR spectrometer with attenuated total reflectance (ATR) by using powdered samples. ATR and baseline corrections were made for all measurements. Nitrogen sorption isotherms for all samples were collected at 77 K using a Micromeritics 3Flex surface area analyzer using ultrahigh-purity (99.999%) gases for analysis (N_2) and free space measurements (He). Prior to measurements all dried samples were transferred to preweighed sample tubes and degassed under vacuum at the respective temperatures mentioned in the Experimental Section of each sample until no change in mass was observed, using a Micromeritics VacPrep sample preparation system. The weight of the sample tube was recorded both after degassing and after the measurement. Pore size distribution was calculated from the N_2 isotherm data using the N2 Tarazona NLDFT model available on the Micromeritics software 3Flex 5.03 version. The regularization parameters applied for each sample were 0.1 (ZrMOP), 1.0 (CuMOP), 1.0 (PdMOP), 0.00316 (UiO-66), 0.00316 (HKUST-1), and 1.0 (Co sponge).

ZrMOP. The synthesis was carried out by slightly modifying a reported literature procedure.[25] Zirconocene dichloride (500 mg, 1.7 mmol) and terephthalic acid (142 mg, 0.85 mmol) were added to a 50 mL round-bottom flask and dissolved in 12.5 mL of DMF. 2.5 mL of deionized water was added into this reaction mixture, and the solution was heated at 60 °C for 20 h in an oil bath. The white precipitate was collected by filtration and washed with DMF (2 × 20 mL) and chloroform (3 × 20 mL) by centrifugation. The solvent was removed by heating at 60 °C under vacuum for 4 h (yield = 88%). ^1H NMR (500 MHz, DMSO-d_6, 25 °C): δ (ppm) = 10.57 (s, 12H, O−H), 7.95 (s, 24H, Ph-H), 6.64 (s, 60H, Cp-H). FTIR (ATR, cm^{-1}): 3106 (w), 1657 (w), 1557 (m), 1506 (w), 1017 (w), 811 (w), 743 (w), 548 (w), 513 (w). PXRD, NMR, TGA, and FTIR spectra are shown in Figures 2, S1, S3, and S4, respectively. Prior to N_2 adsorption measurements, the material was activated at 60 °C for 24 h under vacuum on the VacPrep system.

UiO-66. The synthesis was carried out based on a reported literature procedure.[56] Zirconium(IV) chloride (530 mg, 2.3 mmol) and terephthalic acid (380 mg, 2.3 mmol) were added into a 250 mL round-bottom flask and dissolved in 60 mL of DMF. The solution was heated at 120 °C for 24 h in an oil bath. The white precipitate formed was collected by filtration and washed thoroughly with 300 mL of DMF, then solvent-exchanged overnight with MeOH (3 × 30 mL). The product was collected by centrifugation and dried at room temperature under vacuum to obtain the white solid product. FTIR (ATR, cm^{-1}): 3166 (w), 1657 (w), 1574 (w), 1506 (w), 1392 (m), 1155 (w), 1104 (w), 1019 (w), 880 (w), 812 (w), 745 (w), 658 (w,), 598 (w)). PXRD, TGA, and FTIR spectra are shown in Figures 2, S3 and S4, respectively. Prior to N_2 adsorption measurements, the material was activated at 120 °C for 24 h under vacuum on the VacPrep system.

CuMOP. The synthesis was carried out based on a reported literature procedure.[27] Copper(II) nitrate 2.5 hydrate (425 mg, 1.8 mmol) and isophthalic acid (350 mg, 2.1 mmol) were added to a 100 mL round-bottom flask and dissolved in 20 mL of 3:1 (v/v) DMF/ethanol mixture. The solution was heated in a Teflon vessel inside a parr bomb reactor at 80 °C for 24 h and then at 60 °C for 14 h. The blue-colored solid formed was collected by centrifugation, then solvent-exchanged overnight with DMF (1 × 30 mL) and ethanol (3 × 30 mL) and dried at room temperature under vacuum to remove the solvent (yield = 40%, Mw = 6668.34 g/mol). FTIR (ATR, cm^{-1}): 3278 (w), 2975 (w), 1632 (w), 1551 (w), 1483 (w), 1447 (w), 1389 (m), 1277 (w), 1162 (w), 1079 (w), 1043 (w), 743 (w), 728 (w), 625 (w). PXRD, TGA, and FTIR spectra are shown in Figures 2, S3 and S4, respectively. Prior to N_2 adsorption measurements, the material was activated at 120 °C for 24 h under vacuum on the VacPrep system.

HKUST-1. The synthesis was carried out based on a reported literature procedure.[57] Copper(II) acetate monohydrate (600 mg, 3.0 mmol) was dissolved in 50 mL of deionized water in a 250 mL round-bottom flask. 1,3,5-benzenetricarboxylic acid (420 mg, 1.9 mmol) was added to a 100 mL round-bottom flask and dissolved in 50 mL of ethanol. This solution was carefully poured into a copper(II) acetate solution. A light blue product was immediately formed and crashed out of the solution. Next, a mixture of triethylamine (0.85 mL) and cyclohexane (10 mL) was added dropwise to the reaction mixture.

https://doi.org/10.1021/acs.chemmater.3c03020
Chem. Mater. 2024, 36, 4185−4195

The solution was left to sit at room temperature for 24 h. The blue-colored product was collected by centrifugation, then solvent-exchanged overnight with Milli-Q water (1 × 30 mL) and ethanol (3 × 30 mL). The solvent was removed by drying at 50 °C under vacuum for 12 h. FTIR (ATR, cm^{-1}): 3550 (w), 3165 (w), 2976 (w), 1651 (w), 1618 (w), 1581 (w), 1506 (w), 1483 (w), 1433 (w), 1376 (m), 1092 (w), 1044 (w), 755 (w), 730 (w). PXRD, TGA, and FTIR spectra are shown in Figures 2, S3 and S4, respectively. Prior to N_2 adsorption measurements, the material was activated at 120 °C for 24 h under vacuum on the VacPrep system.

PdMOP. Synthesis was carried out based on reported literature procedures.[58,59]

$PdbpyCl_2$. Palladium chloride (443 mg, 2.5 mmol) was mixed with 25 mL of acetonitrile in a 100 mL round-bottom flask by sonication and heated at 70 °C for 1 h. The hot solution was filtered into a solution of 2,2′-bipyridine (391 mg, 2.5 mmol) in acetonitrile (50 mL) in a 250 mL round-bottom flask. The reaction was stirred overnight, and the solid product was collected by filtration and washed with acetonitrile and acetone. ^{1}H NMR (500 MHz, DMSO-d_6, 25 °C): δ (ppm) = 9.13 (d, 2H, 3,3′ pyridine), 8.58 (d, 2H, 6,6′-pyridine), 8.36 (t, 2H, 4,4′-pyridine), 7.82 (t, 2H, 5,5′-pyridine).

$Pdbpy(ONO_2)_2$. $PdbpyCl_2$ (500 mg, 1.5 mmol) was heated in 140 mL of 1 M HNO_3 to 70 °C. Next, $AgNO_3$ (256 mg, 1.5 mmol) dissolved in a few drops of deionized water was added to the reaction mixture. White-colored AgCl started to precipitate out immediately, and the reaction mixture was allowed to stir overnight. The solid was removed by filtration, and the product in the filtrate was collected by removing the solvent under vacuum. The isolated yellow-colored solid was washed with acetonitrile (6 × 30 mL) by centrifugation. ^{1}H NMR (500 MHz, D_2O, 25 °C): δ (ppm) = 8.35 (m, 2H, 3,3′-bpy), 8.31 (m, 2H, 6,6′-bpy), 8.27 (m, 2H, 4,4′-bpy), 7.74 (m, 2H, 5,5′-bpy).

PdMOP. $Pdbpy(ONO_2)_2$ (60 mg, 0.144 mmol) and 2,4,6-tris(4-pyridyl)-1,3,5-triazine (31 mg, 0.096 mmol) were mixed with 10 mL of 1:1 (v/v) methanol/water mixture in a 50 mL round-bottom flask, and the resulting suspension was heated refluxed at 80 °C overnight. The solid was removed by filtration. The product in the filtrate was collected by removing the solvent under vacuum. The yellow-colored solid was washed with chloroform (3 × 30 mL) and diethyl ether (2 × 30 mL) by centrifugation and dried at 60 °C under vacuum overnight (yield = 65%). ^{1}H NMR (500 MHz, DMSO-d_6, 25 °C): δ (ppm) = 9.63 (d, 24H, pyridine − H_α), 9.07 (d, 24H, pyridine − H_β), 8.63 (d, 12H, 6,6′-bpy), 8.53 (t, 12H, 5,5′-bpy), 7.83(d, 12H, 3,3′-bpy), 7.75 (t, 12H, 4,4′-bpy). FTIR (ATR, cm^{-1}): 3418 (w), 3086 (w), 2962 (w), 2924 (w), 2854 (w), 1668 (w), 1607 (w), 1575 (w), 1520 (m), 1471 (w), 1450 (w), 1372 (m), 1335 (m), 1312 (m), 1159 (w), 1109 (w), 1062 (w), 1042 (w), 811 (w), 770 (w). PXRD, NMR, TGA, and FTIR spectra are shown in Figures 1, S2−S4, respectively. Prior to N_2 adsorption measurements, the material was activated at 60 °C for 24 h under vacuum on the VacPrep system.

Co-Sponge. The synthesis was carried out based on a reported literature procedure.[30] A solution of cobalt(II) thiocyanate (140 mg, 0.8 mmol) dissolved in 20 mL of MeOH was layered on a solution of 2,4,6-tris(4-pyridyl)-1,3,5-triazine (126 mg, 0.4 mmol) dissolved in 100 mL of a 1:4 (v/v) MeOH/o-dichlorobenzene mixture in a 250 mL round-bottom flask. The solution was left to sit at room temperature for 3 weeks. The orange-colored solid formed was collected by filtration, and the color changed rapidly from orange to green with solvent removal. FTIR (ATR, cm^{-1}): 3060 (w), 2053 (m), 1610 (w), 1575 (w), 1515 (m), 1455 (w), 1372 (w), 1316 (w), 1125 (w), 1061 (w), 1033 (w), 1011(w), 800 (w), 748 (w), 650 (w), 513(w). PXRD, TGA, and FTIR spectra are shown in Figures 2, S3 and S4, respectively. Prior to N_2 adsorption measurements, the material was activated at 120 °C for 12 h under vacuum on the VacPrep system.

RESULTS AND DISCUSSION

Synthesis and Structural Characterization. *ZrMOP.* The ZrMOP cage structure has four $[Cp_3Zr_3(\mu_3\text{-}O)(\mu_2\text{-}OH)_3]^{4+}$ metal nodes formed from the hydrolysis of zirconocene dichloride, and six 1,4-benzenedicarboxylate linkers that give rise to a tetrahedral geometry, as shown in Figure 1.[25] Cp groups effectively cap the metal clusters to enforce a convergent polyhedral geometry. The ZrMOP synthesis was carried out following a reported procedure,[25] and ^{1}H NMR (Figure S1) was used to confirm the structure. The synthesized MOP was also characterized by PXRD (Figure 2), TGA (Figure S3), and FTIR spectroscopy (Figure S4).

UiO-66. UiO-66 is a well-established MOF containing $[Zr_6(\mu_3\text{-}O)_4(\mu_3\text{−}OH)_4]^{12+}$ nodes that can be coordinated by up to 12 1,4-benzenedicarboxylate linkers, as shown in Figure 1.[26] The structure contains both tetrahedral and octahedral pore geometries, shown in blue and green, respectively, in Figure 1; ZrMOP replicates only the tetrahedral pore.[60] In an ideal unit cell, there are eight tetrahedral pores (7.5 Å) and four octahedral pores (12 Å).[61,62] The synthesized UiO-66 was characterized by using PXRD (Figure 2), TGA (Figure S3), and FTIR spectroscopy (Figure S4).

CuMOP. The CuMOP comprises 12 Cu−Cu paddlewheel nodes at the vertices bridged by 24 1,3-benzenedicarboxylate linkers resulting in a truncated-cuboctahedral geometry (Figure 1).[27] The CuMOP was characterized by PXRD (Figure 2), TGA (Figure S3), and FTIR spectroscopy (Figure S4).

HKUST-1. Similar to CuMOP, the nodes of HKUST-1 also consist of Cu−Cu paddlewheel nodes. However, in this MOF structure, the use of a tricarboxylate linker instead of the dicarboxylate ligands allows the formation of an extended framework instead of the discrete MOP (Figure 1). HKUST-1 contains three types of pores, two of them similar and larger in size than the third.[63] An ideal unit cell of HKUST-1 contains 8 small pores with a ∼5.4 Å diameter, and 3 and 2 larger pores with 11.1 Å (type I) and 13.1 Å (type II) diameters, respectively.[64] The type I pore with a 11.1 Å diameter resembles the truncated cuboctahedral core of the CuMOP (see Figure 1).[54,64,65] The synthesized product was characterized by PXRD (Figure 2), TGA (Figure S3), and FTIR spectroscopy (Figure S4).

PdMOP. This cage structure has a truncated tetrahedral geometry with six Pd^{2+} nodes at the vertices linked by four 2,4,6-tris(4-pyridyl)-1,3,5-triazine (TPT) ligands on the faces (Figure 1). The coordination sites of Pd metal centers in this MOP are capped by 2,2′-bipyridine groups to give a discrete structure instead of an extended framework. ^{1}H NMR spectroscopy was used to confirm the purity of the synthesized product (Figure S2). In addition, PXRD (Figure 2), TGA (Figure S3), and FTIR (Figure S4) characterizations were performed.

Co Sponge. This coordination polymer consists of truncated tetrahedral subunits with six Co^{2+} metal nodes bridged by four TPT ligands.[30] Each metal vertex is shared by adjacent truncated tetrahedra, giving rise to an extended structure. Each Co metal center is also coordinated by two thiocyanate groups at the axial positions. An analysis of the crystal structure reveals that in addition to the PdMOP-like truncated tetrahedral pores, there are two additional pores that give rise to channels through the framework (see Figure 1).[55] The orange-colored product started turning light green during filtration and a darker green during activation as a result of solvent removal that prompts a phase transition reported to occur on the surface of the crystals.[55,66] The PXRD data supports this phase transition, with significant differences

https://doi.org/10.1021/acs.chemmater.3c03020
Chem. Mater. 2024, 36, 4185−4195

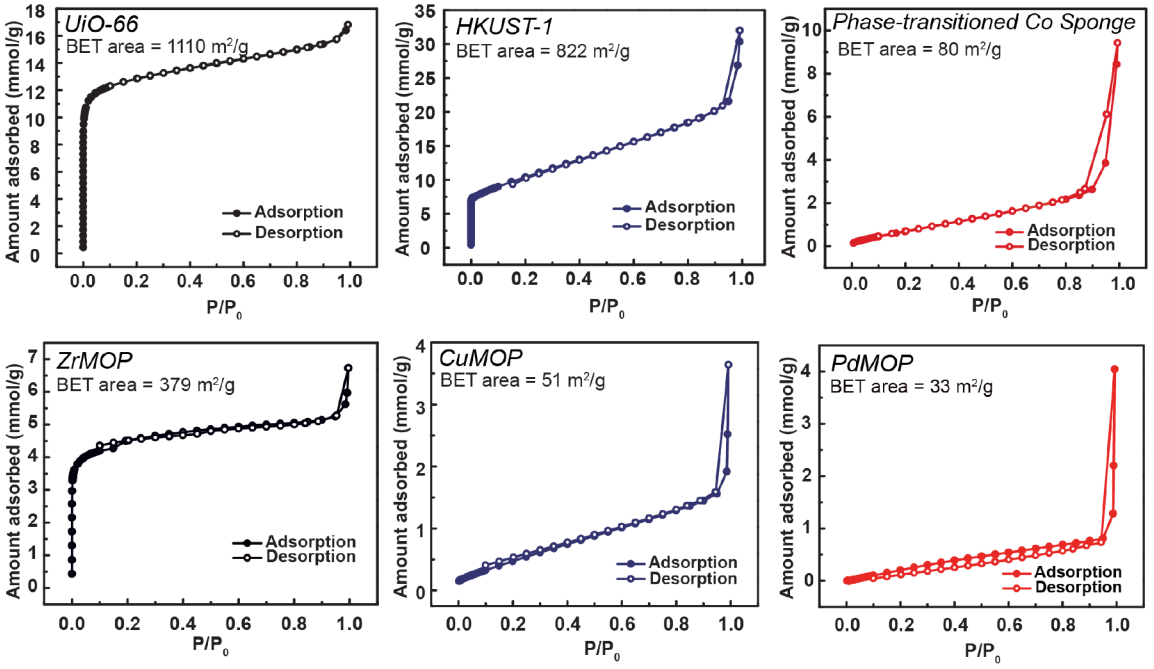

Figure 3. Nitrogen adsorption isotherms of MOF and MOP samples collected at 77 K and their respective BET areas.

between the pre- and postactivation diffractograms. Since the phase transition was reported to be limited to the surface, we carried out PXRD (Figure 2), TGA (Figure S3), and FTIR spectroscopy (Figure S4), along with sorption measurements, anticipating that the core Co Sponge may remain accessible to probing gas molecules.

Surface Area Comparison. N_2 gas sorption studies at 77 K were performed on the six selected MOP and MOF samples. Prior to gas sorption experiments, all powder samples were activated at the respective temperatures and time periods mentioned in the Experimental Section until no further changes in mass were observed. In this study, we selected the BET model for calculating surface areas. When carrying out the calculations, a linear region on the BET plot $(1/[Q(P_0/P - 1)])$ vs P/P_0) was identified by applying the consistency criteria by Rouquerol et al. as listed below.[67,68]

1. Relative-pressure region where $Q(1 - P/P_0)$ is continuously increasing with P/P_0 on the Rouquerol BET plot ($(Q(1 - P/P_0)$ vs P/P_0).
2. A positive BET constant (C) value.
3. The calculated monolayer loading (Q_m) corresponds to a relative pressure that lies within the selected relative pressure range.
4. The relative pressure that corresponds to the monolayer loading (Q_m) should be within a 20% tolerance of that calculated by the BET equation $(1(\sqrt{C} + 1))$.

P/P_0 is the relative pressure, P_0 is the saturation pressure of nitrogen, and C and Q_m are constants corresponding to the energy of adsorption of the first adsorbed layer and the monolayer loading, respectively.

ZrMOP and UiO-66. The ZrMOP showed a Type I isotherm, with a sharp knee in the low-pressure region that is characteristic of microporous materials and is consistent with what is reported in the literature (Figure 3).[25] The calculated BET area was 379 m^2/g (Figures S5, S6). Table S1 indicates data from criteria and conditions used to calculate the BET areas for all samples. The calculated area is lower than what was reported by the initial study on ZrMOP (685 m^2/g).[25] The PXRD pattern of the sample collected after carrying out N_2 sorption measurements indicates a loss of bulk crystallinity (Figure 2). This is commonly observed in MOPs with the removal of solvent molecules during activation that disrupts the long-range order,[69] unless supramolecular interactions are incorporated into the design.[53] A similar loss of sample crystallinity was observed by Yuan and coworkers, and we note that in their sample, the loss of crystallinity was greater than what we observed.[25] The differences in the BET areas for a given cage can be attributed to the degree of bulk crystallinity.[70,71] What is particularly interesting is that typically structural collapse will decrease BET areas for both MOPs and MOFs.[72] For the latter, preserving extended structure is a primary motivation for the design of supramolecular frameworks, where noncovalent interactions preserve extrinsic porosity between cages.[73] However, for some cages where efficient crystal packing blocks the outer faces, a loss of bulk crystallinity may expose the external edges and vertices, increasing the surface available for adsorption and thus increasing its BET area. Work by Snurr and coworkers showing how the accessible surface area measured by rolling a probe molecule on a surface can increase with exposed edges supports this effect.[74] Despite the fact that ZrMOP maintains a significant amount of bulk porosity even upon loss of crystallinity, the sorption properties of this class of cage can be enhanced by the formation of supramolecular frameworks. Choe and coworkers note that when the bridging terephthalic acid is functionalized with an amine group, the crystal packing is significantly different, resulting in extrinsic pores that increased the measured BET area to 782 m^2/g.[53]

N_2 adsorption by UiO-66 also resulted in a Type I isotherm (Figure 3). The BET area calculated for the synthesized UiO-66 was 1110 m^2/g, and this matches closely with literature reported values.[56,61] The PXRD pattern collected after N_2

https://doi.org/10.1021/acs.chemmater.3c03020
Chem. Mater. 2024, 36, 4185−4195

sorption experiments indicates that the bulk crystallinity is preserved even after the removal of solvent molecules during activation. The BET area calculated for the UiO-66 sample was almost three times greater than that determined for our ZrMOP with an analogous tetrahedral pore structure.

BET areas are gravimetric surface areas. The calculated contribution to the BET area by a single pore was determined to be 205.8 $Å^2$/pore for the ZrMOP (data on calculations are provided in Table S2). A calculation for the analogous tetrahedral pores in UiO-66 was carried out, indicating a per-pore surface area of 49.2 $Å^2$/pore. Specific parameters in the following discussion are summarized in Table 1. When

Table 1. Selected Metrics Derived from Sorption Measurements

	ZrMOP	UiO-66	CuMOP	HKUST-1
measured BET area (m^2/g)	379	1110	51	822
BET area per pore ($Å^2$/pore)	205.8	49.2	56.46	194.40
mass required per(analogous) pore (g/pore) × 10^{-22}	54.3	13.5	110.7	58.4
mass required per (any) pore(g/pore) × 10^{-22}	-	9.01	-	13.5
volume required per (analogous) pore ($Å^3$/pore)	4932.03	1116.21	12178.1	6093.3
volume required per (any) pore($Å^3$/pore)	-	744.14	-	1406.15

calculating this value, the presence of both octahedral and tetrahedral pores in UiO-66 was considered, and our value is specific to the latter. Thus, the MOP shows 4.2 times the surface area per pore versus the analogous tetrahedral pores in the MOF and 2.0 times the surface area when compared to the collective tetrahedral and octahedral pores in UiO-66. In the case of an MOP, each building block belongs to a single pore. In an MOF, the building blocks used to frame one pore also contribute structurally to adjacent pores. Since a BET area is determined by sorption of gas molecules, it is not a direct measure of the geometric surface area of a pore. For MOPs, the gas molecules can adsorb not only to the internal surfaces of the building blocks but also externally. For MOFs, the external surface of a building block becomes the internal cavity of the neighboring pore, and so, on a per-pore basis, the number of gas molecules that can be accommodated is lower. However, the shared nature of the building blocks in an MOF that theoretically reduces the area per pore significantly improves the sorption properties on a gravimetric basis. The mass of the building blocks needed to frame a single pore of ZrMOP is 4.02 times the mass attributed to a tetrahedral pore of UiO-66. Furthermore, when the unit cell volumes and number of pores per unit cell are compared, the ZrMOPs have a significantly lower density of pores per volume. UiO-66 has 12 total pores per unit cell of ∼8929.65 $Å^3$, whereas the ZrMOP has four in its unit cell of 19728.1 $Å^3$. Thus, although the ZrMOP area per pore is twice as high (205.8 $Å^2$/pore versus 100.0 $Å^2$/pore), the density of pores in the MOF is ∼6.6 times higher. Therefore, it would take ∼3 times the volume of crystalline ZrMOP to realize the same surface area of UiO-66.

CuMOP and HKUST-1. The N_2 adsorption isotherm measured for the CuMOP looks similar to those shown by analogous CuMOPs.[14,75] It is difficult to strictly classify the shape of this isotherm as belonging to one of the six well-known types of isotherms, and is typically shown when the pores of a given sample are not accessible by the probe molecules.[76,77] The increased adsorption observed at high P/P_0 is indicative of minor interparticle porosity.[78] The calculated BET area for CuMOP was 51 m^2/g. To the best of our knowledge, a BET area for the CuMOP has not been calculated using N_2 adsorption data. However, an estimated Langmuir surface area of 514 m^2/g has been reported using N_2 adsorption data,[3] and a BET area of 13 m^2/g has been reported from H_2 adsorption data.[79] Analogous CuMOPs with similar cuboctahedral geometries, but containing substituted groups at the fifth position on the phenyl ring, have reported BET areas of 17.5 m^2/g($-NH_2$) and 7 m^2/g ($-SO_3Na$).[14,75] The low surface areas measured can be a result of the close packing of the cage molecules or structural collapse upon activation or both, making the pore spaces inaccessible to N_2 molecules, as further supported by the pore size distribution data discussed below. The dependence of surface areas of MOPs on their solid-state packing has been shown previously.[80,81] The N_2 adsorption isotherm measured for HKUST-1 results in a BET area of 822 m^2/g. The very first record of HKUST-1 reports a surface area of 692.2 m^2/g.[28] The majority of BET areas reported in the literature for HKUST-1 fall in the range of 400−1800 m^2/g.[82] As often seen for MOFs, the differences in surface areas reported can arise from activation conditions, defects in the structure, network collapse, as well as methods of calculation used by different researchers.[83]

The surface area per pore of the CuMOP was calculated to be 56.5 $Å^2$/pore, and that for an analogous pore in HKUST-1 was calculated to be 194.4 $Å^2$/pore. In this case, the surface area of an MOP pore is only 0.29 times that of a similar pore in the MOF and so it is not general that an MOP will always have a higher area per pore. Since the BET area of the CuMOP should be similarly advantaged by external sorption, this lower value further indicates that packing of MOPs may limit the accessibility of the carrier gas. Acknowledging that BET areas are not geometric surface areas, it is interesting to note that if the radius of the tetrahedral pore of ZrMOP is taken to be 3.75 Å, the area of such a sphere would be 177 $Å^2$, which is close to the measured BET area per pore.[25] This does not mean the ZrMOP has nearly ideal sorption but rather that adsorption to external surfaces can contribute to the total. In contrast, the 7.5 Å radius of the CuMOP pore results in a geometric area of 706 $Å^2$ yet the area per pore is only 56.5 $Å^2$/pore as a result of pore inaccessability.[27] The significantly different BET areas are interesting given that the ZrMOP has a markedly smaller radius yet has a larger area per pore. The ZrMOP also lost a greater degree of crystallinity upon activation, which is consistent with the hypothesis discussed earlier that when MOP packing is disrupted in a way that does not block pore openings the molecular pores remain intact but surface sites become accessible for sorption. Since the CuMOP remains more crystalline, intermolecular packing can block the accessibility of the carrier gas, reducing BET areas despite the larger internal cavity of the cage.

The lower surface area per pore for the CuMOP as opposed to the analogous pore in HKUST-1 further reinforces that the close intermolecular packing of cage units in crystals of the CuMOP makes the pores inaccessible to gas molecules. Additionally, the mass of building blocks needed to frame a single pore for the MOP is 1.9 and 8.2 times higher than that for a similar and any type of pore in HKUST-1, respectively,

https://doi.org/10.1021/acs.chemmater.3c03020
Chem. Mater. 2024, 36, 4185−4195

directly manifesting in a lower gravimetric surface area of the cage.

PdMOP and Co Sponge. Similar to the CuMOP, the PdMOP also shows very low N_2 adsorption as seen from the isotherm until it reaches a higher relative pressure, when the uptake drastically increases, indicating minor interparticle porosity. The BET area calculated for the PdMOP is 33 m^2/g. The PXRD pattern after the adsorption measurements remained similar to that for the as-synthesized material (Figure 2). The phase-transitioned Co Sponge framework also showed an isotherm similar to that of its analogous MOP. The BET area measured for this material was 80 m^2/g. The low surface area was attributed to a structural collapse reported to occur at the surface of the material that prevents the N_2 molecules from entering the bulk material.[55,74] Densified surface layers preventing accessible pores is a phenomenon that has also been reported for a Zn analogue of HKUST-1.[77] Because the measured areas are not related to the bulk porosity, a comparison of the area per pore is not meaningful.

As described above, MOF pores share vertices and edges with the neighbors. As a simple model to illustrate why shared building blocks enhance the gravimetric area of MOFs but not MOPs, we have used simple cubic pores with 12 edges. When considering a series of cubes (Figure 4A) versus a collection of

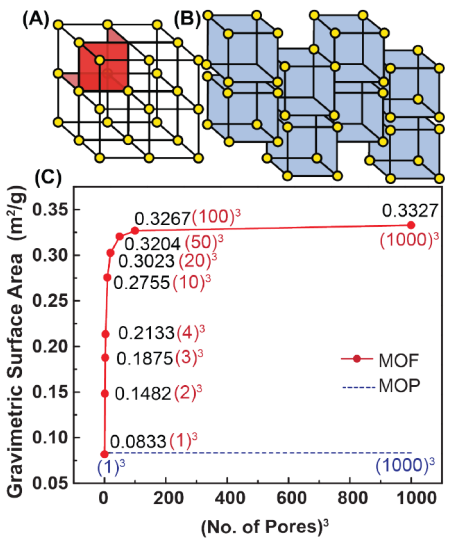

Figure 4. Schematic representation of an ideal (A) MOF and (B) MOP packing. Each cube is considered as a repeat unit. (C) Graphical representation to show how the specific surface areas of MOFs and MOPs change based on their structure and packing into idealized cubes. Red and blue numbers represent the length of the ideal cubes in repeat units for the MOF and MOP, respectively.

the same number of individual cubic pores (Figure 4B), it is straightforward to calculate the gravimetric area after assigning the mass of each edge to 1 g and the surface area of a single cube to 1 m^2. For example, the specific surface area of a single cube unit is 1 m^2/12 g, or 0.0833 m^2/g. When eight pores are arranged as a 2 × 2 × 2 cube, the specific area increases to 0.1482 m^2/g while eight discrete pores remain at 0.0833 m^2/g. As the cubes get larger, there are diminishing returns as the number of internal pores that share all edges become dominant. Since each edge contributes to four different pores, the effective number of edges needed to support a single internal pore is quartered. This can be visualized in Figure 4C where the specific area of the cubes approaches an asymptote at ~4x the specific area of that of the discrete cubic pore (blue dashed line, Figure 4C). Tabulated data for this simple model are provided in Table S4. Our selection of 1 g per edge and area of 1 m^2 is not chemically relevant, but this analysis does align with studies of how the MOF crystal size impacts porosity. In practice, there are additional factors beyond simple geometric analysis that also play a role, as have been described elsewhere.[84]

PORE SIZE DISTRIBUTION

The pore size distributions (PSDs) for all MOP and MOF samples were calculated based on N_2 isotherms collected at 77 K, using an NLDFT model. The PSD of ZrMOP (Figure 5)

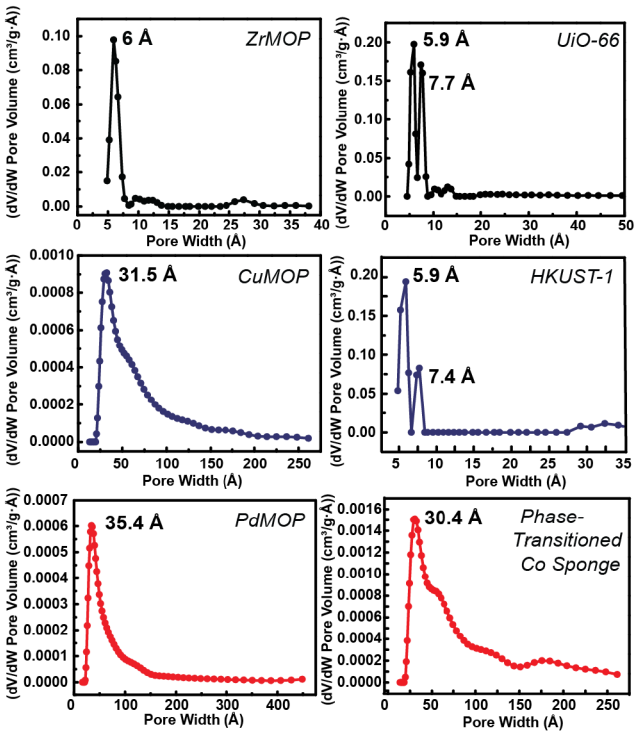

Figure 5. Pore size distribution of the MOF and MOP samples derived from N_2 isotherm data collected at 77 K using a N2 Tarazona NLDFT model.

shows a pore width of 6 Å, which matches with what has been reported for similar cages,[53,85] and a similar pore is found for UiO-66, as expected since the cage matches the tetrahedral pores of the MOF. The experimental PSD for an amine-functionalized ZrMOP that maintains extrinsic porosity via hydrogen bonding to chloride counterions showed similar peaks to the data for UiO-66; in addition to the 6 Å tetrahedral pores, the supramolecular framework shows pores at 10 and 18 Å, which correspond to cubic and rhombicuboctahedral sites.[53] As shown in Figure 5, the data for the unfunctionalized ZrMOP contain only a single significant peak and lack the additional features that indicate the presence of substantial interparticle porosity. An examination of the single-crystal XRD data provided by Yuan and coworkers reveals that although some hydrogen bonding to the chloride counterions occurs, the lack of significant extrinsic pores for this material is due to the formation of 3-fold interpenetrated network that results in close contacts between cages.[25] This is further

https://doi.org/10.1021/acs.chemmater.3c03020
Chem. Mater. 2024, 36, 4185−4195

support for why the loss of crystallinity does not negatively impact the BET area for the ZrMOP, the efficient packing in the solid state blocks interparticle voids and sorption to the outside faces of the cage and thus disrupting this packing has a favorable impact on the gravimetric surface area. A close look at larger pore widths in our ZrMOP data reveals some features that may correspond to extrinsic pores (~13 and 27 Å), but the pore volumes of these peaks are quite small. A loss of crystallinity will disrupt the 3-fold interpenetration and may expose some interparticle voids, but it is clear that these do not contribute significantly to the measured BET area. The PSD of the UiO-66 sample shows clear peaks with pore widths centered around 5.9 and 7.7 Å (Figure 5), indicative of the different pore types in UiO-66. These values agree with previous measurements.[86]

For the CuMOP, we do not see a peak that can be assigned to the intrinsic pore diameter which is expected to be ~15 Å based on the crystal structure.[27] The broad peak around 31.5 Å that tails to very high pore widths and has a very low pore volume is evidence that activation and loss of crystallinity have an opposite effect as what we observed for ZrMOP (Figure 5). Structural collapse may hinder the ability of the probe gas to fully reach the inner cavities of the CuMOP, even though N_2 (3.64 Å) is smaller than the pore apertures of this MOP (8 and 12 Å).[27] As a result, the BET area of this cage is relatively low. We note that cages formed from similar isophthalic acid ligands that bridge 12 M_2 paddlewheel sites may have BET areas that rival those of MOFs.[87] For example, Bloch and coworkers report a value of 1135 m^2/g for a related Cr-based MOP and the PSD data clearly show an intrinsic pore of ~14 Å with no broad features >30 Å, even after activation and a reported loss of crystallinity.[88] The contrast between the CuMOP and CrMOP data further demonstrates that for MOPs, a loss of crystallinity can have two very opposite effects, even for cages that share identical topology. For CuMOP, internal cavities become blocked, and for CrMOP, the intrinsic porosity remains accessible. These effects are significant, given the 51 m^2/g (CuMOP) versus 1135 m^2/g (CrMOP) BET areas. The HKUST-1 sample shows two distinct peaks at 5.9 and 7.4 Å in its PSD (Figure 5), similar to what has been previously reported for this MOF using an NLDFT method.[89]

In both the PdMOP and the phase-transitioned Co Sponge (Figure 5), we see PSDs with broad distributions and very low pore volumes, similar to those of the CuMOP. In addition, they do not show any peaks in the region corresponding to smaller pores. These PSD studies further support that the internal cavities of the PdMOP are inaccessible to the probing gas. Similarly, the phase transition at the surface of the Co Sponge prevents the intrinsic pores from contributing to the data.

CONCLUSIONS

The objective of this study was to perform a direct comparison of the physical properties of selected MOPs with their analogous MOFs. Three MOPs were selected: ZrMOP, CuMOP, and PdMOP. Their nitrogen adsorption isotherms were measured, and BET areas were calculated based on the Rouquerol criteria. These calculated values were then compared to MOF structures with analogous pores: UiO-66, HKUST-1, and Co Sponge. In addition to our experimental measurements of these samples, a few supramolecular frameworks and cages from the literature provided additional context for understanding extrinsic porosity and the effect of a loss of crystallinity. The highest BET area among the MOPs was measured for the ZrMOP, followed by CuMOP and then by PdMOP. Although MOFs show higher BET areas than MOPs in general, we now show that when the surface area is normalized per pore, the value for the ZrMOP is four times higher than that of UiO-66. Our quantitative analysis shows that even when the surface area per pore is larger for MOPs, the shared building blocks in an MOF result in significantly enhanced gravimetric surface areas. Another important conclusion from this work is that a loss of crystallinity does not always correlate with a decrease in the BET area for MOPs. Unlike for MOFs, where framework collapse inherently eliminates pores, for MOPs, the intrinsic porosity persists when the extended packing is disrupted. If the extended cage framework is packed efficiently or interpenetrated, disrupting the crystallinity can enhance BET areas by making the internal cavities accessible and enabling adsorption to the outside faces, which we observed for ZrMOP and has been noted for a CrMOP. On the other hand, structural collapse may block the probe gas from reaching the intrinsic pores, reducing BET area, as we observed for the CuMOP, PdMOP, and Co sponge. The unpredictable nature of a loss of crystallinity can be mitigated by designing noncovalent interactions between cages to form persistent supramolecular frameworks that preserve extrinsic porosity across a wide range of conditions. For applications where a dispersion of single pores is valuable, for example, in thin films or membranes where larger crystallites or aggregates can result in defects, the high surface area per pore of MOPs is attractive. For applications where a high uptake capacity per mass or volume is needed, as for storage, MOFs or supramolecular frameworks are ideal.

ASSOCIATED CONTENT

Supporting Information

The Supporting Information is available free of charge at https://pubs.acs.org/doi/10.1021/acs.chemmater.3c03020.

^{1}H NMR, TGA, FTIR, BET plots, and calculation data; BET consistency criteria and other conditions used when calculating the BET areas (Table S1); surface area comparison calculation data for ZrMOP and UiO-66 (Table S2); surface area per pore calculation data for CuMOP and HKUST-1 (Table S3); tabulated data showing the change in specific surface areas (Table S4); ^{1}H NMR spectrum of ZrMOP (Figure S1), $PdbpyCl_2$, $Pdbpy(ONO_2)_2$, and PdMOP (Figure S2), TGA curves collected under N_2 flow (Figure S3); FTIR spectra of the as-synthesized MOFs and MOPs (Figure S4); $Q(1 - P/P_0)$ vs P/P_0 plot of ZrMOP (Figure S5), UiO-66 (Figure S7), CuMOP (Figure S9), HKUST-1 (Figure S11), PdMOP (Figure S13), Co sponge (Figure S15); BET plot of ZrMOP (Figure S6), UiO-66 (Figure S8), CuMOP (Figure S10), HKUST-1 (Figure S12), PdMOP (Figure S14), Co sponge (Figure S16) (PDF)

AUTHOR INFORMATION

Corresponding Author

Timothy R. Cook − *Department of Chemistry, University at Buffalo, The State University of New York, Buffalo, New York 14260-3000, United States;* orcid.org/0000-0002-7668-8089; Email: trcook@buffalo.edu

https://doi.org/10.1021/acs.chemmater.3c03020
Chem. Mater. 2024, 36, 4185−4195

Authors

Heshali K. Welgama − *Department of Chemistry, University at Buffalo, The State University of New York, Buffalo, New York 14260-3000, United States;* orcid.org/0000-0002-9826-9803

Anish Avasthi − *Department of Chemistry, University at Buffalo, The State University of New York, Buffalo, New York 14260-3000, United States*

Complete contact information is available at: https://pubs.acs.org/10.1021/acs.chemmater.3c03020

Funding

This work was supported by the U.S. Department of Energy National Energy Technology Laboratory (NETL # DEFE0031736) and the National Science Foundation (1847950, 2015723).

Notes

The authors declare no competing financial interest.

■ ACKNOWLEDGMENTS

Nuclear magnetic resonance experiments were carried out at the University at Buffalo's NMR facility using the Bruker AVANCE NEO 500 MHz NMR (NSF CHE-2018160). This research also used resources in the Chemistry Instrument Center (CIC) and the Materials Characterization Laboratory (MCL) in the University at Buffalo.

■ REFERENCES

(1) Cook, T. R.; Zheng, Y.-R.; Stang, P. J. Metal−organic frameworks and self-assembled supramolecular coordination complexes: Comparing and contrasting the design, synthesis, and functionality of metal−organic materials. *Chem. Rev.* **2013**, *113*, 734−777.

(2) Cook, T. R.; Stang, P. J. Recent developments in the preparation and chemistry of metallacycles and metallacages via coordination. *Chem. Rev.* **2015**, *115*, 7001−7045.

(3) Gosselin, A. J.; Rowland, C. A.; Bloch, E. D. Permanently microporous metal−organic polyhedra. *Chem. Rev.* **2020**, *120*, 8987−9014.

(4) Kirchon, A.; Feng, L.; Drake, H. F.; Joseph, E. A.; Zhou, H.-C. From fundamentals to applications: A toolbox for robust and multifunctional MOF materials. *Chem. Soc. Rev.* **2018**, *47*, 8611−8638.

(5) Zhang, Y.; Wu, J.; Zhang, S.; Shang, N.; Zhao, X.; Alshehri, S. M.; Ahamad, T.; Yamauchi, Y.; Xu, X.; Bando, Y. MOF-on-MOF nanoarchitectures for selectively functionalized nitrogen-doped carbon-graphitic carbon/carbon nanotubes heterostructure with high capacitive deionization performance. *Nano Energy* **2022**, *97*, 107146.

(6) Wu, J.; Xuan, X.; Zhang, S.; Li, Z.; Li, H.; Zhao, B.; Ye, H.; Xiao, Z.; Zhao, X.; Xu, X.; et al.et al. N, P-doped carbon nanorings for high-performance capacitive deionization. *Chem. Eng. J.* **2023**, *473*, 145421.

(7) Zhang, Y.; Li, H.; Yang, Q.; Zhang, S.; Zhao, B.; Wu, J.; Shang, N.; Zhao, X.; Xiao, Z.; Zang, X.; et al.et al. Core−shell 2D nanoarchitectures: engineering N, P-doped graphitic carbon/MXene heterostructures for superior capacitive deionization. *J. Mater. Chem. A* **2023**, *11*, 14356−14365.

(8) Pastore, V. J.; Sullivan, M. G.; Welgama, H. K.; Crawley, M. R.; Friedman, A. E.; Rumsey, C.; Trebbin, M.; Rzayev, J.; Cook, T. R. Clickable Norbornene-Based Zirconium Carboxylate Polyhedra. *Chem. Mater.* **2023**, *35*, 1651−1658.

(9) Li, J.-R.; Zhou, H.-C. Bridging-ligand-substitution strategy for the preparation of metal−organic polyhedra. *Nat. Chem.* **2010**, *2*, 893−898.

(10) Mal, P.; Schultz, D.; Beyeh, K.; Rissanen, K.; Nitschke, J. R. An unlockable−relockable iron cage by subcomponent self-assembly. *Angew. Chem.* **2008**, *120*, 8421−8425.

(11) Sullivan, M. G.; Sokolow, G. E.; Jensen, E. T.; Crawley, M. R.; MacMillan, S. N.; Cook, T. R. Altering the solubility of metal−organic polyhedra via pendant functionalization of Cp 3 Zr 3 O (OH) 3 nodes. *Dalton Trans.* **2023**, *52*, 338−346.

(12) Carné-Sánchez, A.; Albalad, J.; Grancha, T.; Imaz, I.; Juanhuix, J.; Larpent, P.; Furukawa, S.; Maspoch, D. Postsynthetic covalent and coordination functionalization of rhodium (II)-based metal−organic polyhedra. *J. Am. Chem. Soc.* **2019**, *141*, 4094−4102.

(13) Liu, J.; Fulong, C. R. P.; Hu, L.; Huang, L.; Zhang, G.; Cook, T. R.; Lin, H. Interpenetrating networks of mixed matrix materials comprising metal-organic polyhedra for membrane CO2 capture. *J. Membr. Sci.* **2020**, *606*, 118122.

(14) Liu, X.; Wang, X.; Bavykina, A. V.; Chu, L.; Shan, M.; Sabetghadam, A.; Miro, H.; Kapteijn, F.; Gascon, J. Molecular-scale hybrid membranes derived from metal-organic polyhedra for gas separation. *ACS Appl. Mater.* **2018**, *10*, 21381−21389.

(15) Xu, S.; Li, S.; Guo, X.; Huang, H.; Qiao, Z.; Zhong, C. Co-assembly of soluble metal−organic polyhedrons for high-flux thin-film nanocomposite membranes. *J. Colloid Interface Sci.* **2022**, *615*, 10−18.

(16) Fulong, C. R. P.; Guardian, M. G. E.; Aga, D. S.; Cook, T. R. A self-assembled iron (II) metallacage as a trap for per-and polyfluoroalkyl substances in water. *Inorg. Chem.* **2020**, *59*, 6697−6708.

(17) Carné-Sánchez, A.; Craig, G. A.; Larpent, P.; Hirose, T.; Higuchi, M.; Kitagawa, S.; Matsuda, K.; Urayama, K.; Furukawa, S. Self-assembly of metal−organic polyhedra into supramolecular polymers with intrinsic microporosity. *Nat. Commun.* **2018**, *9*, 2506.

(18) Tranchemontagne, D. J.; Ni, Z.; O'Keeffe, M.; Yaghi, O. M. Reticular chemistry of metal−organic polyhedra. *Angew. Chem., Int. Ed.* **2008**, *47*, 5136−5147.

(19) Lorzing, G. R.; Gosselin, A. J.; Trump, B. A.; York, A. H.; Sturluson, A.; Rowland, C. A.; Yap, G. P.; Brown, C. M.; Simon, C. M.; Bloch, E. D. Understanding gas storage in cuboctahedral porous coordination cages. *J. Am. Chem. Soc.* **2019**, *141*, 12128−12138.

(20) Olenyuk, B.; Whiteford, J. A.; Fechtenkötter, A.; Stang, P. J. Self-assembly of nanoscale cuboctahedra by coordination chemistry. *Nature* **1999**, *398*, 796−799.

(21) McTernan, C. T.; Davies, J. A.; Nitschke, J. R. Beyond platonic: how to build metal−organic polyhedra capable of binding low-symmetry, information-rich molecular cargoes. *Chem. Rev.* **2022**, *122*, 10393−10437.

(22) Yoshizawa, M.; Klosterman, J. K.; Fujita, M. Functional molecular flasks: new properties and reactions within discrete, self-assembled hosts. *Angew. Chem., Int. Ed.* **2009**, *48*, 3418−3438.

(23) Yeh, R. M.; Xu, J.; Seeber, G.; Raymond, K. N. Large M4L4 (M= Al (III), Ga (III), In (III), Ti (IV)) tetrahedral coordination cages: an extension of symmetry-based design. *Inorg. Chem.* **2005**, *44*, 6228−6239.

(24) Banerjee, R.; Chakraborty, D.; Mukherjee, P. S. Molecular Barrels as Potential Hosts: From Synthesis to Applications. *J. Am. Chem. Soc.* **2023**, *145*, 7692−7711.

(25) Liu, G.; Ju, Z.; Yuan, D.; Hong, M. In situ construction of a coordination zirconocene tetrahedron. *Inorg. Chem.* **2013**, *52*, 13815−13817.

(26) Cavka, J. H.; Jakobsen, S.; Olsbye, U.; Guillou, N.; Lamberti, C.; Bordiga, S.; Lillerud, K. P. A new zirconium inorganic building brick forming metal organic frameworks with exceptional stability. *J. Am. Chem. Soc.* **2008**, *130*, 13850−13851.

(27) Eddaoudi, M.; Kim, J.; Wachter, J.; Chae, H.; O'keeffe, M.; Yaghi, O. Porous metal− organic polyhedra: 25 Å cuboctahedron constructed from 12 Cu2 (CO2) 4 paddle-wheel building blocks. *J. Am. Chem. Soc.* **2001**, *123*, 4368−4369.

(28) Chui, S. S.-Y.; Lo, S. M.-F.; Charmant, J. P.; Orpen, A. G.; Williams, I. D. A chemically functionalizable nanoporous material [Cu3 (TMA) 2 (H2O) 3] n. *Science* **1999**, *283*, 1148−1150.

(29) Kusukawa, T.; Fujita, M. Self-assembled M6L4-type coordination nanocage with 2, 2 '-bipyridine ancillary ligands. facile crystallization and X-ray analysis of shape-selective enclathration of neutral guests in the cage. *J. Am. Chem. Soc.* **2002**, *124*, 13576−13582.
(30) Inokuma, Y.; Arai, T.; Fujita, M. Networked molecular cages as crystalline sponges for fullerenes and other guests. *Nat. Chem.* **2010**, *2*, 780−783.
(31) Xu, N.; Tan, Y.-X.; El-Sayed, E.-S. M.; Yuan, D. Two Zirconium Metal−Organic Cages with S 4 and D 2d Symmetry: Construction and Detection of Antibiotics. *Cryst. Growth Des.* **2022**, *22*, 2768−2773.
(32) Zhang, Y.; Chen, R.-Q.; Wang, S.-T.; Liu, Y.-J.; Fang, W.-H.; Zhang, J. From an aluminum oxo cluster to an aluminum oxo cluster organic cage. *Chem. Commun.* **2023**, *59*, 3411−3414.
(33) Mollick, S.; Fajal, S.; Mukherjee, S.; Ghosh, S. K. Stabilizing metal−organic polyhedra (MOP): Issues and strategies. *Chem. - Asian J.* **2019**, *14*, 3096−3108.
(34) Liu, G.; Di Yuan, Y.; Wang, J.; Cheng, Y.; Peh, S. B.; Wang, Y.; Qian, Y.; Dong, J.; Yuan, D.; Zhao, D. Process-tracing study on the postassembly modification of highly stable zirconium metal−organic cages. *J. Am. Chem. Soc.* **2018**, *140*, 6231−6234.
(35) Samanta, S. K. Metal Organic Polygons and Polyhedra: Instabilities and Remedies. *Inorganics* **2023**, *11*, 36.
(36) Taggart, G. A.; Antonio, A. M.; Lorzing, G. R.; Yap, G. P.; Bloch, E. D. Tuning the porosity, solubility, and gas-storage properties of cuboctahedral coordination cages via amide or ester functionalization. *ACS Appl. Mater.* **2020**, *12*, 24913−24919.
(37) Hong, S.; Oh, M.; Park, M.; Yoon, J. W.; Chang, J.-S.; Lah, M. S. Large H2 storage capacity of a new polyhedron-based metal−organic framework with high thermal and hygroscopic stability.*Chem. Commun.***2009**, 53975399.
(38) Ghosh, A. C.; Legrand, A.; Rajapaksha, R.; Craig, G. A.; Sassoye, C.; Balázs, G.; Farrusseng, D.; Furukawa, S.; Canivet, J.; Wisser, F. M. Rhodium-based metal−organic polyhedra assemblies for selective CO_2 photoreduction. *J. Am. Chem. Soc.* **2022**, *144*, 3626−3636.
(39) Vardhan, H.; Verpoort, F. Metal-Organic Polyhedra: Catalysis and Reactive Intermediates. *Adv. Synth. Catal.* **2015**, *357*, 1351−1368.
(40) Qin, L.-Z.; Xiong, X.-H.; Wang, S.-H.; Meng, L.-L.; Yan, T.-A.; Chen, J.; Zhu, N.-X.; Liu, D.-H.; Wei, Z.-W. A Series of Functionalized Zirconium Metal−Organic Cages for Efficient CO2/N2 Separation. *Inorg. Chem.* **2021**, *60*, 17440−17444.
(41) Zhao, C.; Wang, N.; Wang, L.; Sheng, S.; Fan, H.; Yang, F.; Ji, S.; Li, J. R.; Yu, J. Functionalized metal-organic polyhedra hybrid membranes for aromatic hydrocarbons recovery. *AlChE J.* **2016**, *62*, 3706−3716.
(42) Zhang, D.; Ronson, T. K.; Zou, Y.-Q.; Nitschke, J. R. Metal−organic cages for molecular separations. *Nat. Rev. Chem.* **2021**, *5*, 168−182.
(43) Sokolow, G. E.; Crawley, M. R.; Morphet, D. R.; Asik, D.; Spernyak, J. A.; McGray, A. R.; Cook, T. R.; Morrow, J. R. Metal−Organic Polyhedron with Four Fe (III) Centers Producing Enhanced T1Magnetic Resonance Imaging Contrast in Tumors. *Inorg. Chem.* **2022**, *61*, 2603−2611.
(44) Sepehrpour, H.; Fu, W.; Sun, Y.; Stang, P. J. Biomedically relevant self-assembled metallacycles and metallacages. *J. Am. Chem. Soc.* **2019**, *141*, 14005−14020.
(45) Wu, Z.; Zhou, K.; Ivanov, A. V.; Yusobov, M.; Verpoort, F. The simplest and fascinating metal−organic polyhedra: Tetrahedra. *Coord. Chem. Rev.* **2017**, *353*, 180−200.
(46) Farha, O. K.; Eryazici, I.; Jeong, N. C.; Hauser, B. G.; Wilmer, C. E.; Sarjeant, A. A.; Snurr, R. Q.; Nguyen, S. T.; Yazaydın, A. O. Z. R.; Hupp, J. T. Metal−organic framework materials with ultrahigh surface areas: Is the sky the limit? *J. Am. Chem. Soc.* **2012**, *134*, 15016−15021.
(47) Hönicke, I. M.; Senkovska, I.; Bon, V.; Baburin, I. A.; Bönisch, N.; Raschke, S.; Evans, J. D.; Kaskel, S. Balancing mechanical stability and ultrahigh porosity in crystalline framework materials. *Angew. Chem., Int. Ed.* **2018**, *57*, 13780−13783.
(48) Rowland, C. A.; Lorzing, G. R.; Gosselin, A. J.; Trump, B. A.; Yap, G. P.; Brown, C. M.; Bloch, E. D. Methane storage in paddlewheel-based porous coordination cages. *J. Am. Chem. Soc.* **2018**, *140*, 11153−11157.
(49) Gong, W.; Chu, D.; Jiang, H.; Chen, X.; Cui, Y.; Liu, Y. Permanent porous hydrogen-bonded frameworks with two types of Brønsted acid sites for heterogeneous asymmetric catalysis. *Nat. Commun.* **2019**, *10*, 600.
(50) Argent, S. P.; Da Silva, I.; Greenaway, A.; Savage, M.; Humby, J.; Davies, A. J.; Nowell, H.; Lewis, W.; Manuel, P.; Tang, C. C.; et al.etal. Porous metal−organic polyhedra: Morphology, porosity, and guest binding. *Inorg. Chem.* **2020**, *59*, 15646−15658.
(51) Sava, D. F.; Kravtsov, V. C.; Eckert, J.; Eubank, J. F.; Nouar, F.; Eddaoudi, M. Exceptional stability and high hydrogen uptake in hydrogen-bonded metal− organic cubes possessing ACO and AST zeolite-like topologies. *J. Am. Chem. Soc.* **2009**, *131*, 10394−10396.
(52) Luo, D.; Zhou, X.-P.; Li, D. Beyond Molecules: Mesoporous Supramolecular Frameworks Self-Assembled from Coordination Cages and Inorganic Anions. *Angew. Chem., Int. Ed.* **2015**, *54*, 6190−6195.
(53) Nam, D.; Huh, J.; Lee, J.; Kwak, J. H.; Jeong, H. Y.; Choi, K.; Choe, W. Cross-linking Zr-based metal−organic polyhedra via postsynthetic polymerization. *Chem. Sci.* **2017**, *8*, 7765−7771.
(54) Wu, H.; Simmons, J. M.; Liu, Y.; Brown, C. M.; Wang, X. S.; Ma, S.; Peterson, V. K.; Southon, P. D.; Kepert, C. J.; Zhou, H. C.; et al.et al. Metal−organic frameworks with exceptionally high methane uptake: Where and how is methane stored? *Chem. - Eur. J.* **2010**, *16*, 5205−5214.
(55) Brunet, G.; Safin, D. A.; Korobkov, I.; Cognigni, A.; Murugesu, M. Hidden Transformations of a Crystalline Sponge: Elucidating the Stability of a Highly Porous Three-Dimensional Metal−Organic Framework. *Cryst. Growth Des.* **2016**, *16*, 4043−4050.
(56) Garibay, S. J.; Cohen, S. M. Isoreticular synthesis and modification of frameworks with the UiO-66 topology. *Chem. Commun.* **2010**, *46*, 7700−7702.
(57) Shen, T.; Liu, T.; Mo, H.; Yuan, Z.; Cui, F.; Jin, Y.; Chen, X. Cu-based metal−organic framework HKUST-1 as effective catalyst for highly sensitive determination of ascorbic acid. *RSC Adv.* **2020**, *10*, 22881−22890.
(58) Fulong, C. R. P.; Liu, J.; Pastore, V. J.; Lin, H.; Cook, T. R. Mixed-matrix materials using metal−organic polyhedra with enhanced compatibility for membrane gas separation. *Dalton Trans.* **2018**, *47*, 7905−7915.
(59) Wimmer, S.; Castan, P.; Wimmer, F. L.; Johnson, N. P. Preparation and interconversion of dimeric di-μ-hydroxo and tri-μ-hydroxo complexes of platinum (II) and palladium (II) with 2, 2′-bipyridine and 1, 10-phenanthroline*J. Chem. Soc., Dalton Trans.***1989**, 403412.
(60) Ramsahye, N. A.; Trens, P.; Shepherd, C.; Gonzalez, P.; Trung, T. K.; Ragon, F.; Serre, C. The effect of pore shape on hydrocarbon selectivity on UiO-66 (Zr), HKUST-1 and MIL-125 (Ti) metal organic frameworks: Insights from molecular simulations and chromatography. *Microporous Mesoporous Mater.* **2014**, *189*, 222−231.
(61) Winarta, J.; Shan, B.; Mcintyre, S. M.; Ye, L.; Wang, C.; Liu, J.; Mu, B. A decade of UiO-66 research: a historic review of dynamic structure, synthesis mechanisms, and characterization techniques of an archetypal metal−organic framework. *Cryst. Growth Des.* **2020**, *20*, 1347−1362.
(62) Shankwitz, J.; Speed, D.; Sinanan, D.; Szulczewski, G. The effects of functional groups and missing linkers on the adsorption capacity of aromatic hydrocarbons in uio-66 thin films. *Inorganics* **2021**, *9*, 1.
(63) Hendon, C. H.; Walsh, A. Chemical principles underpinning the performance of the metal−organic framework HKUST-1. *Chem. Sci.* **2015**, *6*, 3674−3683.
(64) Geng, X.; Mao, Y.; Li, S.; Yang, X.; Zhou, B.; Liu, S.; Yang, Z. Water Unexpectedly Impacts Both Thermodynamics and Kinetics of Rn Removal in HKUST-1. *J. Phys. Chem. C* **2023**, *127*, 18149−18158.

https://doi.org/10.1021/acs.chemmater.3c03020
Chem. Mater. 2024, 36, 4185−4195

(65) Hassan, Z. M.; Guo, W.; Welle, A.; Oestreich, R.; Janiak, C.; Redel, E. Formation of Gold Nanoclusters from Goldcarbonyl Chloride inside the Metal-Organic Framework HKUST-1. *Molecules* **2023**, *28*, 2716.
(66) Fulong, C. R. P.; Cook, T. R. Sequestration of orange G and methylene blue from aqueous solutions using a Co (ii) coordination polymer. *RSC Adv.* **2017**, *7*, 26532−26536.
(67) Rouquerol, J.; Llewellyn, P.; Rouquerol, F. Is the BET equation applicable to microporous adsorbents. *Stud. Surf. Sci. Catal.* **2007**, *160*, 49−56.
(68) Islamoglu, T.; Idrees, K. B.; Son, F. A.; Chen, Z.; Lee, S.-J.; Li, P.; Farha, O. K. Are you using the right probe molecules for assessing the textural properties of metal−organic frameworks? *J. Mater. Chem. A* **2021**, *10*, 157−173.
(69) Chen, T.-H.; Wang, L.; Trueblood, J. V.; Grassian, V. H.; Cohen, S. M. Poly (isophthalic acid)(ethylene oxide) as a Macromolecular Modulator for Metal−Organic Polyhedra. *J. Am. Chem. Soc.* **2016**, *138*, 9646−9654.
(70) Sánchez-González, E.; Tsang, M. Y.; Troyano, J.; Craig, G. A.; Furukawa, S. Assembling metal−organic cages as porous materials. *Chem. Soc. Rev.* **2022**, *51*, 4876−4889.
(71) Stacey, P.; Kauffer, E.; Moulut, J.-C.; Dion, C.; Beauparlant, M.; Fernandez, P.; Key-Schwartz, R.; Friede, B.; Wake, D. An international comparison of the crystallinity of calibration materials for the analysis of respirable α-quartz using X-ray diffraction and a comparison with results from the infrared KBr disc method. *Ann. Occup. Hyg.* **2009**, *53*, 639−649.
(72) Grünker, R.; Bon, V.; Müller, P.; Stoeck, U.; Krause, S.; Mueller, U.; Senkovska, I.; Kaskel, S. A new metal−organic framework with ultra-high surface area. *Chem. Commun.* **2014**, *50*, 3450−3452.
(73) Bojdys, M. J.; Briggs, M. E.; Jones, J. T. A.; Adams, D. J.; Chong, S. Y.; Schmidtmann, M.; Cooper, A. I. Supramolecular Engineering of Intrinsic and Extrinsic Porosity in Covalent Organic Cages. *J. Am. Chem. Soc.* **2011**, *133*, 16566−16571.
(74) Düren, T.; Millange, F.; Férey, G.; Walton, K. S.; Snurr, R. Q. Calculating geometric surface areas as a characterization tool for metal− organic frameworks. *J. Phys. Chem. C* **2007**, *111*, 15350−15356.
(75) Sun, L.-B.; Li, J.-R.; Lu, W.; Gu, Z.-Y.; Luo, Z.; Zhou, H.-C. Confinement of metal−organic polyhedra in silica nanopores. *J. Am. Chem. Soc.* **2012**, *134*, 15923−15928.
(76) Sing, K. S. Reporting physisorption data for gas/solid systems with special reference to the determination of surface area and porosity (Recommendations 1984). *Pure Appl. Chem.* **1985**, *57*, 603−619.
(77) Feldblyum, J. I.; Liu, M.; Gidley, D. W.; Matzger, A. J. Reconciling the discrepancies between crystallographic porosity and guest access as exemplified by Zn-HKUST-1. *J. Am. Chem. Soc.* **2011**, *133*, 18257−18263.
(78) Liu, L.; Chen, Z.; Wang, J.; Zhang, D.; Zhu, Y.; Ling, S.; Huang, K.-W.; Belmabkhout, Y.; Adil, K.; Zhang, Y.; et al.et al. Imaging defects and their evolution in a metal−organic framework at sub-unit-cell resolution. *Nat. Chem.* **2019**, *11*, 622−628.
(79) Yang, J.; Lutz, M.; Grzech, A.; Mulder, F. M.; Dingemans, T. J. Copper-based coordination polymers from thiophene and furan dicarboxylates with high isosteric heats of hydrogen adsorption. *CrystEngcomm* **2014**, *16*, 5121−5127.
(80) Bloch, W. M.; Babarao, R.; Schneider, M. L. On/off porosity switching and post-assembly modifications of Cu 4 L 4 metal−organic polyhedra. *Chem. Sci.* **2020**, *11*, 3664−3671.
(81) Zhou, M.; Liu, G.; Ju, Z.; Su, K.; Du, S.; Tan, Y.; Yuan, D. Hydrogen-bonded framework isomers based on Zr-metal organic cage: Connectivity, stability, and porosity. *Cryst. Growth Des.* **2020**, *20*, 4127−4134.
(82) Chen, Y.; Mu, X.; Lester, E.; Wu, T. High efficiency synthesis of HKUST-1 under mild conditions with high BET surface area and CO2 uptake capacity. *Prog. Nat. Sci.: Mater. Int.* **2018**, *28*, 584−589.
(83) Osterrieth, J. W. M.; Rampersad, J.; Madden, D.; Rampal, N.; Skoric, L.; Connolly, B.; Allendorf, M. D.; Stavila, V.; Snider, J. L.; Ameloot, R.; et al.etal. How reproducible are surface areas calculated from the BET equation? *Adv. Mater.* **2022**, *34*, 2201502.
(84) Wang, J.; Imaz, I.; Maspoch, D. Metal− organic frameworks: Why make them small? *Small Struct.* **2022**, *3*, 2100126.
(85) Nam, D.; Kim, J.; Hwang, E.; Nam, J.; Jeong, H.; Kwon, T.-H.; Choe, W. Multivariate porous platform based on metal-organic polyhedra with controllable functionality assembly. *Matter* **2021**, *4*, 2460−2473.
(86) Shan, B.; McIntyre, S. M.; Armstrong, M. R.; Shen, Y.; Mu, B. Investigation of missing-cluster defects in UiO-66 and ferrocene deposition into defect-induced cavities. *Ind. Eng. Chem. Res.* **2018**, *57*, 14233−14241.
(87) Lorzing, G. R.; Gosselin, A. J.; Trump, B. A.; York, A. H. P.; Sturluson, A.; Rowland, C. A.; Yap, G. P. A.; Brown, C. M.; Simon, C. M.; Bloch, E. D. Understanding Gas Storage in Cuboctahedral Porous Coordination Cages. *J. Am. Chem. Soc.* **2019**, *141*, 12128−12138.
(88) Lorzing, G. R.; Trump, B. A.; Brown, C. M.; Bloch, E. D. Selective Gas Adsorption in Highly Porous Chromium(II)-Based Metal−Organic Polyhedra. *Chem. Mater.* **2017**, *29*, 8583−8587.
(89) Kar, A. K.; Srivastava, R. An efficient and sustainable catalytic reduction of carbon−carbon multiple bonds, aldehydes, and ketones using a Cu nanoparticle decorated metal organic framework. *New J. Chem.* **2018**, *42*, 9557−9567.

https://doi.org/10.1021/acs.chemmater.3c03020
Chem. Mater. 2024, 36, 4185−4195